INSTABILITIES IN THREE-DIMENSIONAL SIMULATIONS OF ASTROPHYSICAL JETS CROSSING TILTED INTERFACES

JAGBIR S. HOODA AND PAUL J. WIITA

Department of Physics and Astronomy, Georgia State University, Atlanta, Georgia 30303-3083;
hooda@chara.gsu.edu, wiita@chara.gsu.edu

ABSTRACT

Three-dimensional numerical simulations of light supersonic hydrodynamic jets have been performed to quantify the crucial roles of the interstellar medium (ISM) and intracluster medium (ICM) in defining the gross morphologies of powerful radio galaxies. Such a jet emerges through a power-law atmosphere (ISM) of its host galaxy and then crosses into a hotter, but less dense, ICM. Our eight medium-resolution simulations are followed to lengths of 45 initial jet radii. Simulations with different jet velocities, jet densities, extensions of the ISM (along the jet's axis), and inclination angles of the ISM/ICM interface are compared.

The shear layer between the jet and the shock-processed gas is affected by nonlinear hydrodynamical instabilities. Complex patterns of asymmetric vortex rings and superposed streamwise vortex tubes arise in the cocoon, while internal shocks form in the jet. The low–Mach number jets have higher growth rates of instabilities, in comparison with higher Mach number jets, and the Mach disks or "working surfaces" at the heads of the jets break down. The growth of Rayleigh-Taylor instabilities along the contact discontinuity between the shocked ambient plasma and the shocked jet's plasma appears to trigger the entrainment of heavier external gas into the jet. Greater tilts of the interface induce more wiggling and ribboning of the jets, but none of these simulations evinces substantial jet bending.

Subject headings: galaxies: jets — hydrodynamics — instabilities — intergalactic medium — radio continuum: galaxies

1. INTRODUCTION

Powerful radio sources that grow to distances exceeding ~ 100 kpc over times of $\sim 10^7$ yr must plow through their galaxy's interstellar medium (ISM) into a hot and diffuse intracluster medium (ICM). Most of these powerful sources are classified as Fanaroff-Riley type II radio galaxies (FR II), with small opening angles, often symmetrically placed knots, bright outer hot-spots, and extended lobes. A combination of analytical calculations and two-dimensional numerical simulations have clearly shown a link between hydrodynamical instabilities in light supersonic jets and many observed features in FR II sources (e.g., Norman et al. 1982; Norman & Winkler 1985; Hardee 1987; Chakrabarti 1988; Clarke et al. 1992). Differences in the ambient medium and the jets' interactions with it can also be used to investigate the parameters of the external gas (e.g., Wiita, Rosen, & Norman 1990, hereafter WRN; Wiita & Norman 1992; Hooda, Mangalam, & Wiita 1994; Daly 1994, 1995; Nath 1995). The ambient medium also combines with the jets to determine the morphologies of other classes of radio galaxies and quasars; e.g., wide-angle tail sources (WATs; e.g., Loken et al. 1995), compact steep-spectrum sources (CSSs; e.g., Gopal-Krishna & Wiita 1991; DeYoung 1993; Saikia et al. 1995, 1997), and weak headed quasars (Gopal-Krishna, Wiita, & Hooda 1996; Wiita, Hooda, & Gopal-Krishna 1997).

Recently, well-tested three-dimensional numerical codes and faster supercomputers have provided numerical astrophysicists with the opportunity to build models that allow better comparisons with observations. A number of controlled three-dimensional simulations, using both periodic boundary conditions (e.g., Bassett & Woodward 1995) and free-outflow boundary conditions (Hardee, Clarke, & Howell 1995), provide reasonably good support for the linear perturbative approaches (e.g., Payne & Cohn 1985; Hardee 1987; Birkinshaw 1991; Zhao et al. 1992a). All of these studies provided additional impetus for the simulation of the progress of numerical jets that pass through the hot atmosphere seen around elliptical galaxies (e.g., Forman, Jones, & Tucker 1985), from which the powerful FR II radio sources emerge. Recently, propagating jets have been simulated at moderate resolution using three-dimensional hydrodynamics by Clarke (1996a, 1996b) and Norman (1996); this work has revealed features and nonlinear instabilities, including intermittance of the working surface, not detected in earlier two-dimensional computations.

Our simulations are designed to investigate the growth of various hydrodynamical instabilities in the jet body and at the contact surfaces between the jet, the shocked jet material (cocoon), and the shocked ambient medium. Initial three-dimensional simulations using relatively low resolutions have been described in Hooda & Wiita (1996; hereafter Paper I), and a more extensive description of our approach is given there. Because these jets must begin in galaxies, nearly isothermal atmospheres with essentially power-law drops in density with radius are assumed, as revealed by X-ray emission (Forman et al. 1985; Canizares, Fabbiano, & Trinchieri 1987). We break the axisymmetry in the direction of propagation of the jet in a gentle way, by allowing the normals to the ISM/ICM interfaces to be inclined with respect to the jet axis, as opposed to forcing driving wiggles at the origin (as was done by Hardee et al. 1992, 1995). Other key assumptions of our work are that the variable-density ISM, and the hotter, isothermal ICM, are in pressure equilibrium with each other, and that the ICM can be treated as a constant-density external medium (CDEM). The former is justified by some of our earlier papers (Gopal-Krishna & Wiita 1987; WRN), and the

TABLE 1

SIMULATION PARAMETERS

Run	M_j	η	θ	b	z_H	t_{int}	t_{end}
L1........	6.0	0.0316	0°	0.75	10.0	1.30	4.20
L2........	6.0	0.0316	10°	0.75	10.0	1.30	4.18
L3........	6.0	0.0316	30°	0.75	10.0	1.30	4.19
L4........	6.0	0.0316	45°	0.75	10.0	1.30	3.98
L5........	6.0	0.0100	30°	0.75	10.0	1.06	3.29
L6........	3.0	0.0316	30°	0.75	10.0	3.02	10.03
L7........	3.0	0.0100	30°	0.75	10.0	2.31	8.50
M1.......	6.0	0.0316	30°	0.75	10.0	1.24	4.60
M2.......	6.0	0.0316	30°	CDEM	none	5.68[a]	9.54
M3.......	6.0	0.0316	30°	0.75	30.0	5.30	7.36
M4.......	3.0	0.0316	30°	0.75	10.0	3.12	12.48
M5.......	6.0	0.0316	45°	0.75	10.0	1.24	4.62
M6.......	6.0	0.0316	30°	0.60	30.0	5.08	7.04
M7.......	6.0	0.0100	30°	0.75	10.0	1.08	4.66
M8[b]......	3.0	0.0316	30°	0.75	40.0	7.28	8.00

[a] When $z = 30$.
[b] Nonzero half-opening angle of $\phi = 5°$.

latter, while not strictly true, should be a good approximation over the relatively short distances (less than 50 kpc) that we can consider in these fairly high-resolution three-dimensional computations (Daly 1995).

In § 2 the features of the numerical hydrodynamic code we used, ZEUS-3D, are briefly summarized, and in § 3 we describe the ranges of parameters considered. We present our results in § 4. Our conclusions and some caveats comprise § 5.

2. NUMERICAL SETUP

Our simulations have employed the well-tested, general-purpose three-dimensional code, ZEUS-3D, v.3.4 (Clarke & Norman 1994; Clarke 1996a), an extension of the two-dimensional code ZEUS-2D, which is described in depth in Stone & Norman (1992a, 1992b) and Stone, Mihalas, & Norman (1992). The incarnation of ZEUS-3D that we use is an explicit Eulerian finite-difference code employing the piecewise parabolic advection method (PPA) of Collela & Woodward (1983). Shock waves are treated using the von Neumann–Richtmyer prescription for artificial viscosity. The algorithms used in these codes have been tested extensively against a variety of flow problems in which the solution is either known analytically or has been determined experimentally (Stone & Norman 1992a; Clarke 1996a). The code works well in most situations, but gives small errors for shocks inclined at angles to the grids. Some additional details are given in Paper I.

Our simulations were carried out on the Pittsburgh Supercomputer Center Cray Y-MP C90, and postprocessing was performed using the Fortner TRANSFORM and NCAR interactive graphical software packages. The initiating subroutines for the atmospheres and interfaces were written separately, in order to allow for the density gradient in an isothermal ISM with a tilted interface. The density within the ISM follows

$$\rho(x, y, z) = \frac{\rho_0}{\{1.0 + [(z/z_{scale})z_H/(z_H - x \tan \theta)]^2\}^b}.$$

On crossing the tilted interface at $z = z_H - x \tan \theta$, where z_H is a multiple (usually 10 or 30) of the initial jet radius, R_0 (which defines the length scale), the density drops to $0.2\rho(z_H)$, but the temperature rises by a factor of 5 to

provide a pressure-matched boundary; the density and pressure of the external ambient medium are then kept constant for $z > z_H - x \tan \theta$. In this work the important parameters are the jet Mach number $M_j = u/a_j$, where a_j is the jet sound speed, $\eta \equiv \rho_{jet}/\rho_0$, and the angle θ at which the interface is tilted with respect to the normal to the jet. For all of our simulations, we assume that the jet's initial pressure matches that of the ISM at $z = 0$; however, the possibility of overpressured jets is worth considering in future efforts. We have usually chosen $z_{scale} = 8.9$ for $z_H = 10.0$, or $z_{scale} = 26.7$ for $z_H = 30.0$, and $b = 0.75$, corresponding to the beginning of a power-law decline of ~ 1.5 in density with distance in the ISM (cf. Forman et al. 1985; WRN). For a canonical value of $R_0 = 1$ kpc, our Galaxy extends 10–40 kpc in radius, and if $T_{ISM} = 10^7$ K (a typical value for halo gas), then one time unit corresponds to 2.6×10^6 yr.

3. INPUT PARAMETERS

Our first two-dimensional simulation paper of jets crossing interfaces (WRN) contains a discussion of the reasons for the choice of the parameter ranges that we are investigating. Analytical approximations for the flow through isothermal halos and the speed with which the heads of the jets propagate across the interface have also been presented in previous publications (Wiita & Norman 1992; Hooda et al. 1994; Paper I), where they were shown to agree reasonably well with the numerical work. As no major differences among the comparisons between computational and analytical results found in those earlier efforts and those arising from these new simulations were seen (other than those produced by the continuing growth of instabilities, which render the analytical comparisons less valid), we do not present any of that material here, and we refer the reader to those earlier works for details.

Our new three-dimensional simulations were run on $250 \times 80 \times 80$ active zones, extending out to $45R_0$ along the initial direction of propagation, z, and to $\pm 12R_0$ in both directions perpendicular to it. To provide adequate resolution in the most important region, 28 uniform zones span the jet diameter. The central 32×32 zones, across the x- and y-directions, are equally spaced over distances of $2.4R_0 \times 2.4R_0$ in the x-y plane, whereas the remaining 48 zones (24 on each side, from $\pm 1.2R_0$ to $\pm 12.0R_0$) are

ratioed by a factor of 1.3346, with the smallest zone being equal to $0.075R_0$. Outflow boundary conditions are used everywhere, except for the zones at which the jet fluid is introduced.

These medium-resolution simulations are denoted by M1–M8 in Table 1, which describes the parameters of both these new simulations and those discussed in Paper I (denoted by L1–L7). The last two columns give the times taken by the bow shocks preceding the jets to reach the interfaces (t_{int}) and the end of the grids (t_{end}). For simulation M2, where no halo was employed, and the jet propagated through a CDEM throughout, the time at which the bow shock in front of the jet reached $z = 30R_0$ is quoted in lieu of t_{int}. Run M8 differs from the others in having a nonzero opening angle; the half-opening angle for this case is $\phi = 5°$; another difference is that $x_{scale} = 20$.

The main difference between the L and M sets of simulations is that the low-resolution runs were performed on $150 \times 50 \times 50$ grids, extending on to $35R_0$ along z, and had only 14 zones across the initial jet diameter (see Paper I for details). There is no denying the desirability of simulations of even higher resolution, employing faster Mach numbers and lower jet densities, all of which would improve the match between these models and the expected physical parameters of radio jets. However, all of those desiderata carry substantial penalties in CPU and/or memory usage, precluding their implementation at this time. Each of the current simulations required ~ 35–40 C90 service units.

4. RESULTS

All of these simulations retain the supersonic character of the flow, and the bow shock defines the boundary between the stationary ambient medium (both within the halo and in the ICM) and the fluid affected by the onrushing jet. In agreement with two-dimensional and lower resolution three-dimensional computations, a Mach disk quickly forms at the head of the jet, and the jet fluid is strongly shocked upon passing through it. In all of these simulations, we see that large-scale eddies and substantial backflows arise within the cocoon once the jet has propagated just to $z \approx M_j r_j/2$ (with lengths expressed in terms of R_0), as is also noted by Clarke (1996b). We find that the backflow is concentrated within a roughly annular region with $2 < r/R_0 < 3$ (although it is definitely nonaxisymmetric), with the cocoon flow that is closer to the jet being mostly dragged along with the jet. Both Kelvin-Helmholtz (K-H) and Rayleigh-Taylor (R-T) instabilities clearly develop along the boundaries between the shocked ambient medium and the shocked jet material (cocoon), and at the interface between the jet and the cocoon.

Nonaxisymmetric features become obvious by the time the jets have propagated 5–10 times their original radii. As also seen by Clarke (1996a) and Norman (1996), for light supersonic jets propagating in a CDEM, these departures from axial symmetry become intense, and the jet can be described as flailing about within the cocoon by the time $z \approx 5M_j$. Under these circumstances, the Mach disk can temporarily disappear and re-form in significantly different positions. At some times the jets attain ribbonlike cross sections, and at others they effectively bifurcate, as higher order fluting instabilities now dominate, and there is little remnant of the original axisymmetry. Within the cocoon we

see the formation of smaller eddies and vortex tubes that are precursors of three-dimensional turbulence (Arnold & Arnett 1986; Loken et al. 1996; Norman 1996; Paper I).

One difference between the low-resolution simulations examined in Paper I and those newly described here is that for the standard $M_j = 6$ simulations, the higher resolution runs tend to propagate forward a little faster, at least for $\eta = 0.0316$ (compare t_{int} values for L3/M1 and L4/M5, which are identical, other than for the resolution used). Within ISMs extending only $10R_0$ in length, the finer resolution seems to allow the ratio of the working surface to jet area to stay a bit smaller, thereby concentrating the thrust and allowing a slightly faster progress of the head. But for $\eta = 0.001$ (L5/M7), the t_{int} values are essentially the same. And for the $M_j = 3$, $\eta = 0.0316$ cases (L6/M4), the higher resolution run is slower, which may be explained as arising from the ability to capture the development of the shorter instability scale lengths at low Mach numbers in the higher resolution run. Note that the t_{end} values in Table 1 correspond to different distances ($35R_0$ for L simulations and $45R_0$ for M), but, if measured at the same distances, these trends continue to hold. Another important difference is that the higher resolution simulations allow us to resolve higher order instabilities, and we can see a faster growth of nonaxisymmetric modes.

We now turn to brief descriptions of the features seen within these simulations that are sensitive to the different parameters that we have considered.

4.1. Jet Velocity M_j

Here we examine differences between simulations M1 and M4, which are identical except for M_j values of 6.0 and 3.0, respectively. Obviously, the lower Mach number case takes longer to reach the interface. The distance at which instabilities grow to significance is certainly shorter for $M_j = 3.0$, and this distance does appear to be roughly proportional to the input jet velocity. The slower jet develops a relatively broader cocoon at the same propagation distance and a somewhat higher ratio of working surface to jet area ratio as well. All of these results imply that the time needed to propagate to a given distance, both within the halo and in the CDEM, scales with a power of M_j^{-1} greater than unity; i.e., to reach the interface at $z = 10$, the M4 jet takes 2.5 times as long as does the M1 jet, and to reach the end of the grid at $z = 45$, the M4 jet takes 2.7 times as long. These two simulations are illustrated in Figure 1 (Plate 5).

Examination of cross-sectional slices through the jets shows that the circular cross section near the potential core develops small spikes on its surface that grow into polyhedral shapes downstream. Eventually, oscillations between ribbonlike structures and amoeba-like structures are seen. By the time the jets have reached the ends of the grids, bifurcation and even trifurcation have afflicted them, supporting the "dentist-drill" model (Scheuer 1982; Norman 1996). Cross-sectional slices through the jet show more warping and amorphousness in the $M_j = 3$ case (at similar distances along the jet, but at longer times, of course), as seen in Figure 2 (Plate 6). The jet is also typically located more off-center for the lower velocity case. Instabilities examined in this way also grow faster for case M4 than for M1; similar degrees of distortion are seen at 60%–70% of the length along M4. A ribbonlike mode dominates for much of the M4 simulation, while higher modes, producing a more amoeba-like cross section, are more important for

M1 (Fig. 1). Also shown in the bottom row of Figure 1 is a cross section from simulation M7, which differs from M1 in having a lower jet density and where a somewhat broader jet and cocoon can be seen at the same time and spatial location (see § 4.2).

In all cases a large eddy forms first on the top side of the jet (where it emerges first through the tilted interface; see Paper I). This interacts with the jet to bend it downward, but subsequent eddies spawned on the bottom side tend to push the jet back up, thereby providing the major impetus for apparently random side-to-side wiggling. Asymmetries in the cocoon after crossing the interface are also much greater for the $M_j = 3$ simulation, so this case suffers wiggles with larger amplitude. For case M4 the cocoon eddies are larger, slower, and able to exert greater influence on the jet motion; the streaming/counterstreaming seen within the $M_j = 6$ cocoon is not present. This also shows that the vortex roll-up and vortex pairing (the prime mechanism for eddy generation; Ho & Huerre 1984 and references therein) are suppressed for situations involving greater compressibility, which correspond to higher Mach numbers.

4.2. Jet Density η

Simulation M7 differs from the canonical case, M1, only in having a jet density that is a factor of $10^{1/2}$ smaller. The key difference, seen already in two-dimensional simulations (Norman et al. 1982), is that the lower value of η yields a broader cocoon. We note that the jet in M7 reaches the interface about 13% sooner than does the jet in M1, and the jets reach the end of the grid at very similar times in simulations M1 and M3. This result is counterintuitive, in that the lower density should imply a weaker thrust. A similar result (for L7/L3) was explained in Paper I by noting that with our assumption of pressure balance with the ambient medium, a lower density implies a higher sound speed in the jet medium, so the same Mach number corresponds to a higher physical velocity and actually a higher thrust. The last panels of Figure 1 illustrate the faster velocities seen in the lower density jet. A comparison of the pressure fields at the ends of the simulations M1 and M7 (and also M5) are given in Figure 3 (Plate 7).

Examining the jet within the ISM, we see that the first confinement shock forms more quickly and is closer to the orifice where the jet fluid enters the grid for M7 than for M1. Overall, M7 is more unstable to fluting modes. The lower density jet stays somewhat better confined in these early stages, and this even remains the case once the interface has been crossed.

We can examine the nonlinear surface waves propagating outward along the boundary between the jet and cocoon material. Such waves probably encompass the effects of shear-layer (K-H) instabilities and vortices that cannot be clearly resolved within the current grid, but are expected from analytical work (Hall & Smith 1991). While they are best seen in animations of the flow, to some degree one can see these features in density contour plots (cf. Fig. 5). Measuring the motion of these surface waves in units of the velocity of advance of the jet head, v_h, we find speeds typically around $(2-3)v_h$ for the $\eta = 0.0316$ cases and $(5-7)v_h$ for $\eta = 0.01$. The animations of these jets show that the surface waves arise from complicated feedback from the pressure inhomogeneities of their respective cocoons and/or shear layers, and they cannot be obviously described in terms of body or surface modes of nonpropagating analytically trac-

table jets (see e.g., Payne & Cohn 1985; Hardee 1987; Hardee et al. 1991; Zhao et al. 1992a).

Nonetheless, it is interesting to compare these numerical results with the most thorough analytical approximation of which we are aware, which involves locating complex modes for slab-symmetric jets (Zhao et al. 1992a). (In the limit of small wavenumbers, the wave speeds of these complex modes provide approximate phase velocities of the disturbances of an axisymmetric jet.) The dominant growing waves can be thought of as arising from the slower acoustic waves propagating parallel to the interface, with velocity $v_b = (M_j - 1)a_j$ for Mach numbers that are not too large (e.g., Zhao et al. 1992a, 1992b). To allow comparison with our simulations, we can use the standard analytical estimate for the propagation speed of the jet: $v_h = M_j a_j \eta^{1/2}/(1 + \eta^{1/2})$ (e.g., Norman & Winkler 1985). We ignore the effects of the jet's acceleration and the density gradient within the ISM, as they only provide corrections of $\lesssim 10\%$ to the jet's propagation speed (cf. Hooda & Wiita 1996; Hooda et al. 1994). Then, for the $\eta = 0.0316$ and $\eta = 0.01$ cases for $M_j = 6.0$, the speed of the acoustic body waves in units of the velocity of advance of the jet head are predicted to be 5.5 and 9.2, respectively. These are both somewhat higher than we see, although the trend with η is correct. According to Zhao et al. (1992a), two of the six surface waves should move at $v_{s\pm} = M_j a_j \eta_c^{1/2} (\eta_c^{1/2} \pm 1)^{-1}$ (where η_c is the ratio of the jet to cocoon density). For the plus case, this gives

$$v_{s+} = v_h \left(\frac{\eta_c}{\eta}\right)^{1/2} \frac{1 + \eta^{1/2}}{1 + \eta_c^{1/2}}, \qquad (1)$$

which is independent of M_j, while for the minus case,

$$v_{s-} = v_h \left(\frac{\eta_c}{\eta}\right)^{1/2} \frac{1 + \eta^{1/2}}{\eta_c^{1/2} - 1}. \qquad (2)$$

By using an average value of $\eta_c \approx 1$, obtained from our simulations, we obtain $v_{s+}/v_h \simeq 3.3$ for $\eta = 0.0316$, and $v_{s+}/v_h \simeq 5.5$ for $\eta = 0.01$. Thus, the agreement of the analytical approximation for the surface waves with our numerical results is reasonable. This approximation also predicts large values for v_{s-}, manifestations of which, however, are not identified in these simulations. The other acoustic and surface waves move with speeds outside the range of the nonlinear wave speeds that we can manage to measure confidently in our animations, and they therefore do not have signatures that are quite as visible as those of the waves considered above.

4.3. Interface Tilt θ

All of these higher resolution simulations that go through an ISM have had a nonzero value of θ, and the only case that we have considered in which $\theta \neq 30°$ is M5, where $\theta = 45°$. Otherwise, this simulation is the same as M1. A comparison of late-stage pressure images appears in Figure 3. It is clear that pressure variations extend farther into the cocoon in this case. Paper I contains a fairly extensive discussion of the effects of varying the tilt angle, and we have seen nothing in these new simulations that vitiates those conclusions. In particular, a higher value of θ induces more side-to-side motion in the jet, as the cocoon eddy on the top side is stripped more quickly, so the eddy on the bottom can push the jet back up in the opposite direction sooner than for less severe tilts.
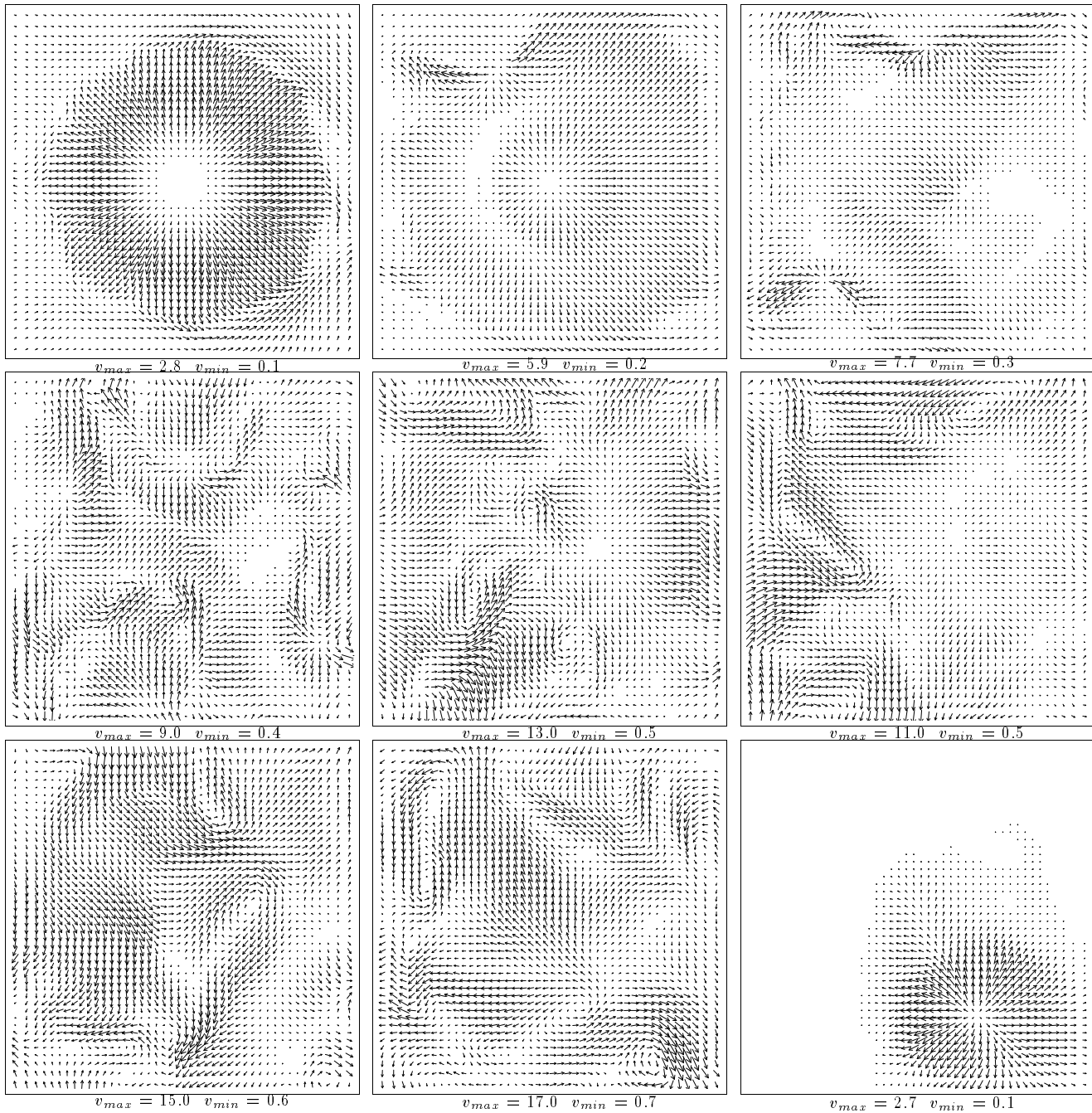
FIG. 4.—The x- and y-components of the velocity vector fields in the x-y plane for run M5 ($M_j = 6.0$, $\eta = 0.0316$, $z_H = 10.00R_0$, $\theta = 45°$, $b = 0.75$) at $t = 4.60$. Each image is $3.11R_0 \times 3.11R_0$ wide. The distances (along the jet's axis) for the left, center, and right images in the upper panel are $4.50R_0$, $9.54R_0$, and $14.58R_0$, respectively. For the middle panel they are $19.62R_0$, $24.66R_0$, and $29.70R_0$, respectively. For the bottom panel they are $34.74R_0$, $39.78R_0$, and $44.82R_0$, respectively. The first slice is dominated by the expansion in the jet core, and the last by expansion from an off-centered bow shock; all the others mainly show the development of eddies in the cocoon.

The twisting of the backflow in the cocoon is very clearly seen in simulation M5, indicating how vortices are beginning to yield turbulence in the cocoon. The overall widths of the cocoons are very similar, as are the rates of advance of the jet/cocoon across the grid. The reconfinement shock in simulation M1 is nearly symmetric for a 30° tilt of the interface, but clearly asymmetric for the $\theta = 45°$ tilt of the interface in simulation M5. The R-T instabilities in the cocoons affect the bending of the jet itself.

In examining cross-sectional slices, we also see that stronger instabilities are induced by greater tilts; M5 shows ribboning and narrowing of the jet occurring sooner than

for M1. Figure 4 illustrates velocity vectors in cross sections through the jet and cocoon for M5 near the end of its simulation. Multiple spikes on the jet sides form first, and they grow at the interface between counterrotating streamwise vortex tubes and azimuthal vortex rings. The helicities in these features gain strength and lead to fire-hose–type instabilities, producing asymmetric shocks within the body of the jet, which in turn drive the twisting of the jet. Finally the jet position jumps around, simulating the "dentist-drill" scenario of Scheuer (1982). In both cases the jets end up with very noncircular cross sections and go through stages in which they have clearly bifurcated.
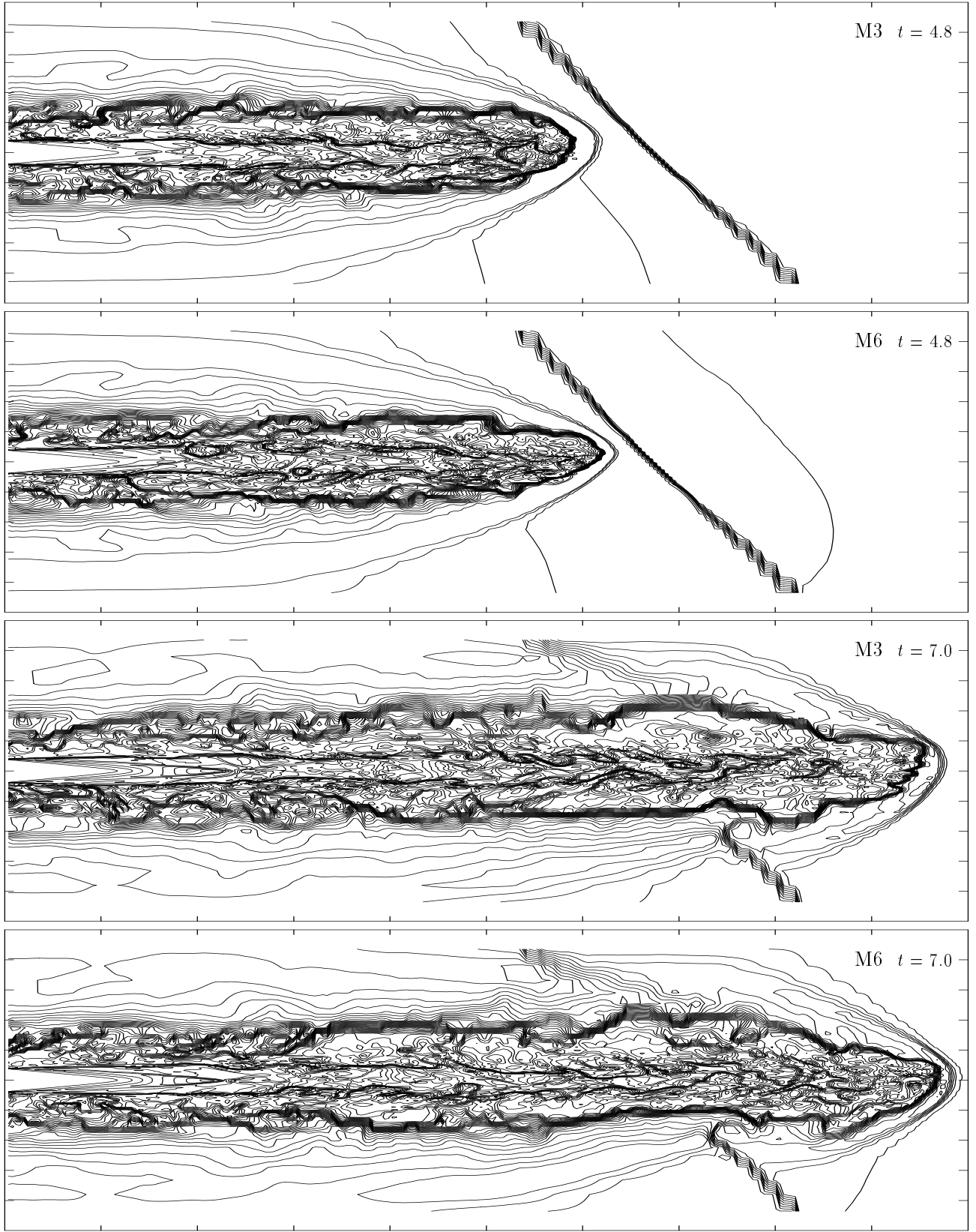
FIG. 5.—Logarithmic density contours for runs M3 ($b = 0.75$) and M6 ($b = 0.60$); $M_j = 6.0$, $\eta = 0.0316$, $z_H = 30.00R_0$, and $\theta = 30°$ are common. Flows through these different power laws are compared at $t = 4.80$ (*top*) and 7.00 (*bottom*). The cuts are through the x-z plane with $y = 0$. Tick marks along the z axis are at intervals of $4.5R_0$, while those along the x-axis are at intervals of $2.67R_0$.

4.4. Distance z_H Traveled within the ISM

When we compare simulations M3 and M1, which are identical, except for the ISM extending 3 times as far for the former, we immediately notice the obvious result that M3 takes longer to get out to a given distance (for $z > 10R_0$), because the extended ISM is denser than the ICM. As we watch this extended evolution within the ISM, we see clear nonaxisymmetries developing by $z \approx 15$, and intermittance in the position of the jet head sets in by $z \approx 25$—before the tilted interface is reached (see Fig. 5). While propagating through this longer halo, a quasi-smooth expansion of the cocoon thickness is seen, which is similar to our results for long two-dimensional simulations (Hooda et al. 1994). The runs with $z_H = 10$ spend too little time within the ISM to show this effect.

Looking within the jet we note that the first conical internal shock never weakens in M3 (as it does in M1), because in M3 the pressure inhomogeneities in the cocoon do not become as weak as they do in M1. Since the low-density CDEM in M3 begins further out, in comparison with that of M1, the rapid inflation of the cocoon on crossing the interface for M3 engenders only weak rarefaction waves, far downstream of the internal shock; whereas in the M1 case, stronger rarefaction waves allow a rapid decay of the internal shocks formed earlier in the ISM. The pressure inhomogeneities, on the other hand, can be interpreted in terms of the nonlinear coherent structures in the cocoon of the jet. (The coherent structures usually evolve from shear layer instabilities; cf. Ho & Huerre 1984 and references therein.) Owing to these instabilities, the jet/cocoon boundary layer is more jagged for M3 than for M1 at similar distances. When we follow nonlinear surface waves along the jet/cocoon boundary, we find them traveling at 4–5 times the rate of the head's advance, and some of them actually catch up with the hot-spot before losing coherence. In this case the agreement with the analytical approximation (Zhao et al. 1992a; cf. § 4.2) to the dominant slower acoustic wave ($\sim 5.5v_h$) looks better than that with the dominant surface wave, v_{s+} ($\sim 3.3v_h$). The waves between the cocoon and the shocked ambient medium propagate slowly backward. Where these two classes of counterflowing waves interact in the cocoon, we find ringlike eddies and shear structures producing vortex tubes. When the output of these simulations is viewed from various perspectives, one can see how the flows twist through the coherent structures of vortex rings and vortex tubes in the cocoon. If we had been able to perform simulations of yet higher resolution, we would expect to resolve smaller eddies that drive weak shocks into the jet.

4.5. Power Law b of the ISM

Here we compare M3 to M6 and M2, in that M6 has a more shallow power-law decline in the ISM, and M2 retains a constant density throughout its ambient medium. Differences between M3 (with $b = 0.75$) and M6 (with $b = 0.60$) are illustrated in Figure 5. Departures from axisymmetry are somewhat smaller for M6 than for M3 at the same times (or distances traveled). We were surprised to see that the jet in M6 reaches the interface (and the end of the grid as well) sooner than does the jet of M3, even though the halo density in the latter falls off faster. The explanation for this peculiar result seems to be that the M6 jet is slightly better confined and less unstable. Thus, the ratio of the area of the working surface to the jet cross-sectional area grows more slowly, and the jet head can propagate a bit faster. This may well be understood as arising from the relatively smoother backflow in the M6 simulation, which would engender less turbulence and tend to produce better collimation. We note that this result might not hold true at lower Mach numbers, but we have not performed a simulation that addresses this question.

Unsurprisingly, the jet propagating through the CDEM (M2) takes the longest to reach a particular distance, as the jet is fighting its way through higher external densities, once away from the origin. Substantial asymmetries and some jet disruption are clear by $z \approx 25$, even though no explicit asymmetries have been introduced. There is no systematic widening of the cocoon in this case, probably because the backflow is relatively fast, as the sideways expansion of the cocoon is suppressed by the higher density external medium. This situation has been considered by Norman (1996), using a different code at similar effective resolution and grid size, and our simulations show most of the features described in that paper: (a) the cocoon is characterized by many small-scale eddies; (b) coherent structures, which form in the cocoon during the initial phase, tend to disintegrate and bring in erratic asymmetric fluctuations in the direction of jet's propagation; (c) by the time it nears the end of the grid, the jet becomes more disturbed, and the cross sections of the jet and the working surface degenerate, producing "dentist-drill" morphologies.

4.6. Opening Angle φ

Simulation M8 differs from all of the others in the values of more than one parameter, so clean comparisons are difficult. It has $M_j = 3.0$, but a very long halo ($z_H = 40$) and a different value of $z_{scale} = 35.6$. We note that the jet expansion continues to $z \approx 15$. Beyond this point the rarefaction wave beyond the reconfinement shock acts to suppress the jet's sideways expansion, and the flow stays quasi-cylindrical thereafter (cf. WRN and Wiita & Norman 1992 for two-dimensional analyses). As for M3 and M6, the cocoon continues to expand throughout the jet's trip through the halo.

We see clear evidence of vortex roll-up at the interface between the cocoon and the shocked ambient medium during the early phase of expansion (see features labeled as A, B, and C in the top panel of Fig. 6). A quasi-stationary axisymmetric conical shock surrounds the potential core (i.e., the conical region, enclosed by the Mach surface, originating at the base of the jet). This confinement shock is primarily excited by the axisymmetric initial and boundary conditions at the origin of the jet. As the jet expands, because of its initial opening angle, conical rarefaction fans move inward, thereby causing a pressure drop behind them. Since the ambient medium was pressure-matched at the inlet, the pressure gradient produced by the rarefaction fans makes the jet boundary curve and sends a conical shock downstream. After passing through the conical shock, the jet flares, affected by both small-scale and large-scale nonlinear fluting instabilities, and the cocoon swells to a diameter of greater than $20R_0$, with a large radius vortex ring being visible at the head of the cocoon (Fig. 6). Vortex pairing and merging follows the initial expansion phase; the interactions of vortices are visible at the interface between the cocoon and the shocked ambient medium, as shown in the middle panel of Figure 6. The formation of vortices also enhances the entrainment of external gas into the main flow.
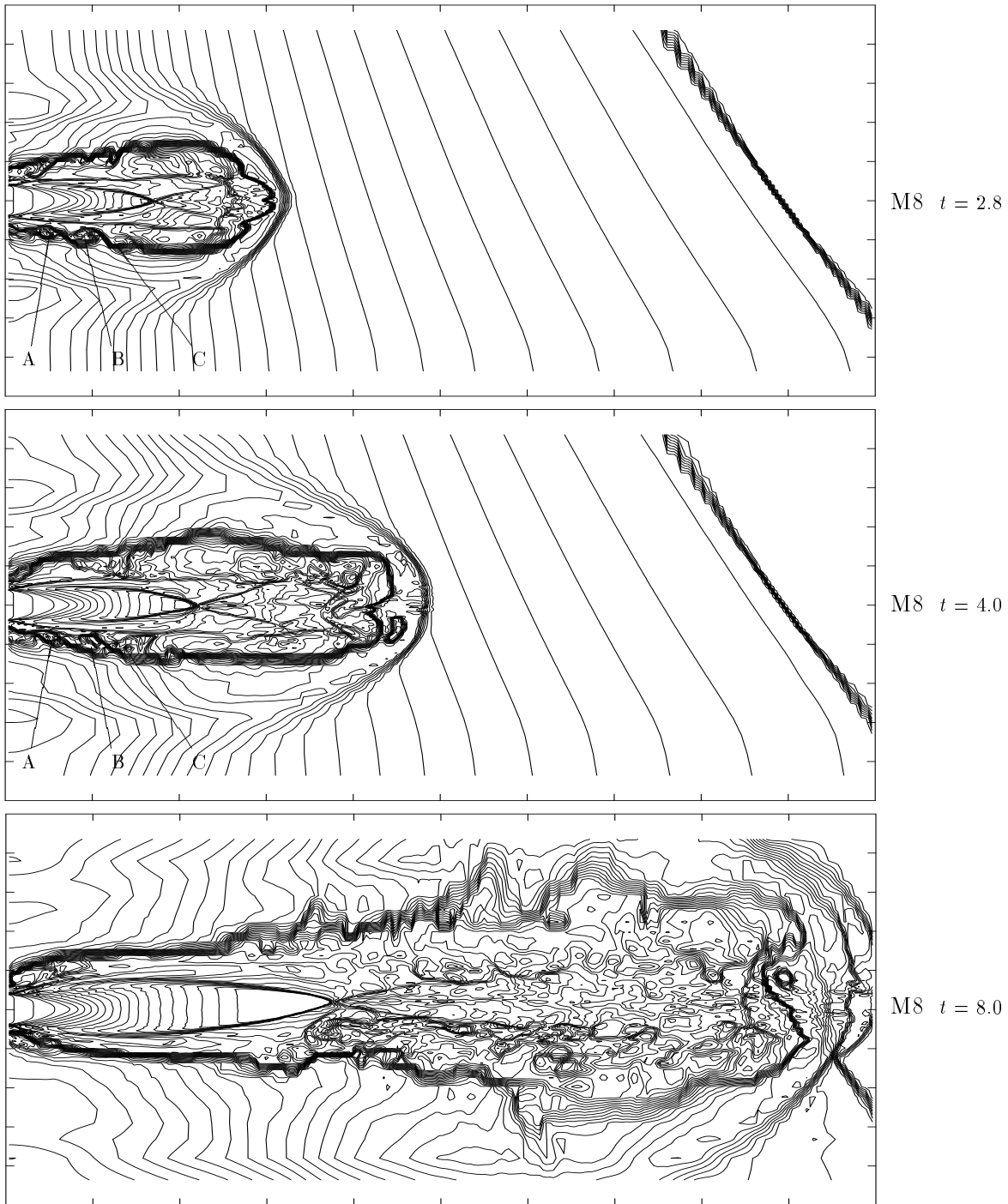
FIG. 6.—Logarithmic density contours for run M8 ($M_j = 3.0$, $\eta = 0.0316$, $\theta = 30°$, $b = 0.75$, and $z_H = 40.00R_0$), with opening angle $\phi = 5°$, are compared at $t = 2.80$ (*top*), $t = 4.00$ (*middle*), and $t = 8.00$ (*bottom*). Merging features referred to in the text are labeled A, B, and C. The cuts and tick marks are as in Fig. 5.

Once entrained, the vortices dissipate, and the flow slows down.

Such expanding jets with decaying working surfaces appear to have relevance for the small set of radio-loud quasars with morphologies characterized by jets without hot-spots on one side and lobes with weak or absent jets on the other—the weak headed quasars (Gopal-Krishna et al. 1996; Wiita et al. 1997). By decreeing a substantial opening angle, these weakened working surfaces can be forced to occur rather quickly in the simulations, but they probably occur for other, more realistically collimated, flows at much later times (which cannot yet be followed in three-

dimensional runs, because of the outlandish computational resources such lengthy simulations would require). The flaring and expansion of these jets suppress the formation of strong shocks, and therefore, this type of jet may well have a steeper power law for synchrotron emission, and it may also be associated with more diffuse FR I–type morphologies, instead of the edge-brightened morphologies of FR II sources. We hope to address these points through forthcoming simulations that include magnetic fields.

5. CONCLUSIONS AND DISCUSSION

We begin with a summary of the conclusions drawn from

the low-resolution simulations (cf. Paper I), some of which agree with earlier two-dimensional work, and some of which are only revealed when axisymmetry is broken.

1. Qualitatively, decreasing the jet density produces a broader cocoon.

2. The stronger internal shocks in the higher density (η) jets make them slower, when compared to analytical results, than are the jets of lower η.

3. Internal shocks are usually induced by the localized pressure perturbations from the vortices; both the shocks and the vortices decay with time.

4. The toroidal cocoon near the Mach disk is comprised of a number of eddies with opposite helicities in the adjoining eddies.

5. The fingerlike growth of the R-T instabilities along the discontinuity of the cocoon and the shocked ambient medium dominate the eventual collapse of the cocoon and the consequent exposure of the jet.

6. Lower Mach numbers yield more internal structure for simulations that are compared at the same distances of propagation. The cocoon's interactions with the jet play a larger role in the slower jets.

7. Increasing the angle of the interface induces more wiggles and asymmetry in the jet propagation, but no significant long-term deflection of the jet occurs. This is expected for simulations without sideways pressure gradients or ICM winds.

8. None of these (L1–L7) jets have completely broken up or become clearly unstable in these lower resolution simulations.

Our medium-resolution simulations (M1–M8) confirm most of the above results, but the additional time and distance to which they were followed allow us to see more instabilities develop in the jets and cocoon. Further, the higher resolution allows us to resolve some important features that were only hinted at in the earlier numerical results.

9. The Mach disks temporarily disappear and re-form, with the working surface becoming intermittent, and the jet becoming decollimated. This conclusion is similar to that obtained in other recent three-dimensional simulations performed at similar resolutions (Norman 1996; Clarke 1996b).

10. The primary and secondary vortices, as well as vortex tubes in the cocoon, are more prominent in these medium-resolution runs. If magnetic fields were to be incorporated, these features should be relevant to the filaments seen in many cocoons (cf. Clarke 1996a). It is very likely that these structures are important in engendering turbulence and entrainment (cf. Loken et al. 1996).

11. The deflection of the jet resulting from crossing a tilted interface is more smooth and prominent for the $M_j = 3$ case than for $M_j = 6$ (M1, M4).

12. Having the ISM/ICM interface closer to the jet's orifice helps in stretching the first conical internal shock out to a longer distance, but it also weakens it (M1, M3), thereby helping the jet to maintain a quasi-cylindrical cross section.

13. Internal shocks are strongest for the steepest power law (M3 vs. M6, M2), so side-to-side oscillations are also more prominent.

14. The collapse of the cocoon into a narrow sheath around the jet within the ISM occurs faster for steeper power laws. The steeper pressure gradient suppresses the backflow in the cocoon more efficiently.

15. Comparing runs with different η (M1, M7), we note that the first internal shock near the orifice converges to the jet's axis faster for M7; the stronger divergence after this shock helps explain why the cocoon is broader for the lower density jet.

16. The fingerlike R-T instabilities between the cocoon and shocked ambient medium are blunter for lower η.

17. The jet's flow in the CDEM, after the reconfinement shock, is more ribbonlike for the case with the greater tilt (M1, M5).

18. The shape of the R-T instabilities are also sharper for higher θ.

Although these simulations were explicitly designed to model flows on the large scale, with the first power-law medium corresponding to galactic ISM and the second external medium corresponding to an ICM, all of these parameters can be freely scaled. Therefore, our simulations could also have relevance to jets emerging from plausible denser media in the nuclei of galaxies, if the physical parameters are all compressed by factors of $\sim 10^4$ (i.e., jets with radii of 0.1 pc, emerging through clouds extending only a few parsecs). In this case, the substantial instabilities seen to grow rapidly in the jets and cocoons might be related to the bending and rapid variations seen in emission from nuclear jets. Such a direct scaling is difficult to justify, however, because two features that have not been incorporated in our computations are expected to play far greater roles on nuclear scales than on full galactic scales: relativistic motions and magnetic fields.

Over the past few years, two-dimensional codes incorporating special relativity for fluid motion, and sometimes also for radiation transport, have been designed. They have now been applied to simulations of shocks moving rapidly in flows designed to mimic those in the nuclei of galaxies (e.g., Gómez et al. 1996; Hughes, Duncan, & Mioduszewski 1996; Komissarov & Falle 1996; Martí et al. 1996). Magnetic fields are probably not dynamically important for the large-scale structure of the great majority of radio sources, as they produce morphologies (e.g., large "nose cones") that are rarely observed (Clarke, Norman, & Burns 1986; Clarke 1996a; Hardee 1996). But most theoretical models for the production of nuclear jets demand the dominance of magnetic fields (e.g., Appl 1996; Christodoulou, Contopoulos, & Kazanas 1996; Lovelace & Romanova 1996). The only work of which we are aware that combines treatments of special relativity and magnetohydrodynamics is that of van Putten (1996). This is an exciting breakthrough, but it is limited so far to two dimensions.

We are currently performing simulations using the MHD capabilities of Zeus 3-D to examine the effects of relatively weak magnetic fields of different initial topologies on the stability and morphology of jets propagating through atmospheres and crossing interfaces.

REFERENCES

Arnold, C. N., & Arnett, W. D. 1986, ApJ, 305, L57
Appl, S. 1996, in ASP Conf. Ser. 100, Energy Transport in Radio Galaxies and Quasars, ed. P. E. Hardee, A. H. Bridle, & J. A. Zensus (San Francisco: ASP), 129
Bassett, G. M., & Woodward, P. R. 1995, ApJ, 441, 582
Birkinshaw, M. 1991, MNRAS, 252, 505
Canizares, C. R., Fabbiano, G., & Trinchieri, G. 1987, ApJ, 312, 503
Chakrabarti, S. K. 1988, MNRAS, 235, 33
Christodoulou, D. M., Contopoulos, J., & Kazanas, D. 1996, in ASP Conf. Ser. 100, Energy Transport in Radio Galaxies and Quasars, ed. P. E. Hardee, A. H. Bridle, & J. A. Zensus (San Francisco: ASP), 37
Clarke, D. A. 1996a, ApJ, 457, 291
———. 1996b, in ASP Conf. Ser. 100, Energy Transport in Radio Galaxies and Quasars, ed. P. E. Hardee, A. H. Bridle, & J. A. Zensus (San Francisco: ASP), 311
Clarke, D. A., Bridle, A. H., Burns, J. O., Perley, R. A., & Norman, M. L. 1992, ApJ, 385, 173
Clarke, D. A., & Norman, M. L. 1994, LCA Preprint 7 (Univ. of Illinois, Urbana-Champaign)
Clarke, D. A., Norman, M. L., & Burns, J. O. 1986, ApJ, 311, L63
Collela, P., & Woodward, P. R. 1983, J. Comput. Phys., 54, 174
Daly, R. A. 1994, ApJ, 426, 38
———. 1995, ApJ, 454, 580
De Young, D. S. 1993, ApJ, 402, 95
Forman, W., Jones, C., & Tucker, W. 1985, ApJ, 293, 102
Gómez, J. L., Martí, J. M., Marscher, A. P., Ibáñez, J. M., & Marcaide, J. M. 1996, in ASP Conf. Ser. 100, Energy Transport in Radio Galaxies and Quasars, ed. P. E. Hardee, A. H. Bridle, & J. A. Zensus (San Francisco: ASP), 159
Gopal-Krishna, & Wiita, P. J. 1987, MNRAS, 226, 531
———. 1991, ApJ, 373, 325
Gopal-Krishna, Wiita, P. J., & Hooda, J. S. 1996, A&A, 316, L13
Hall, P., & Smith, F. T. 1991, J. Fluid Mech., 227, 641
Hardee, P. E. 1987, ApJ, 313, 607
———. 1996, in ASP Conf. Ser. 100, Energy Transport in Radio Galaxies and Quasars, ed. P. E. Hardee, A. H. Bridle, & J. A. Zensus (San Francisco: ASP), 273
Hardee, P. E., Clarke, D. C., & Howell, D. A. 1995, ApJ, 441, 644
Hardee, P. E., Cooper, M. A., Norman M. L., & Stone, J. M. 1992, ApJ, 399, 478
Hardee, P. E., Norman, M. L., Koupelis, T., & Clarke, D. A. 1991, ApJ, 373, 8
Ho, C.-M., & Huerre, P. 1984, Annu. Rev. Fluid Mech., 16, 365

Hooda, J. S., Mangalam, A. V., & Wiita, P. J. 1994, ApJ, 423, 116
Hooda, J. S., & Wiita, P. J. 1996, ApJ, 470, 211 (Paper I)
Hughes, P., Duncan, C., & Mioduszewski, A. 1996, in ASP Conf. Ser. 100, Energy Transport in Radio Galaxies and Quasars, ed. P. E. Hardee, A. H. Bridle, & J. A. Zensus (San Francisco: ASP), 137
Komissarov, S. S., & Falle, S. A. E. G. 1996, in ASP Conf. Ser. 100, Energy Transport in Radio Galaxies and Quasars, ed. P. E. Hardee, A. H. Bridle, & J. A. Zensus (San Francisco: ASP), 165
Loken, C., Burns, J. O., Bryan, G., & Norman, M. 1996, in ASP Conf. Ser. 100, Energy Transport in Radio Galaxies and Quasars, ed. P. E. Hardee, A. H. Bridle, & J. A. Zensus (San Francisco: ASP), 261
Loken, C., Roettiger, K., Burns, J. O., & Norman, M. 1995, ApJ, 445, 80
Lovelace, R. V. E., & Romanova, M. M. 1996, in ASP Conf. Ser. 100, Energy Transport in Radio Galaxies and Quasars, ed. P. E. Hardee, A. H. Bridle, & J. A. Zensus (San Francisco: ASP), 25
Martí, J. M., Font, J. A., Ibáñez, & Müller, E. 1996, in ASP Conf. Ser. 100, Energy Transport in Radio Galaxies and Quasars, ed. P. E. Hardee, A. H. Bridle, & J. A. Zensus (San Francisco: ASP), 149
Nath, B. B. 1995, MNRAS, 274, 208
Norman, M. L. 1996, in ASP Conf. Ser. 100, Energy Transport in Radio Galaxies and Quasars, ed. P. E. Hardee, A. H. Bridle, & J. A. Zensus (San Francisco: ASP), 319
Norman, M. L., Smarr, L. L., Winkler, K.-H. A., & Smith, M. D. 1982, A&A, 113, 285
Norman, M. L. & Winkler, K.-H. A. 1985, Los Alamos Science, 12, 38
Payne, D. G., & Cohn, H. 1985, ApJ, 291, 655
Saikia, D. J., Jeyakumar, S., Wiita, P. J., & Hooda, J. S. 1997, in preparation
Saikia, D. J., Jeyakumar, S., Wiita, P. J., Sanghera, H. S., & Spencer, R. E. 1995, MNRAS, 276, 1215
Scheuer, P. A. G. 1982, in IAU Symp. 97, Extragalactic Radio Sources, ed. D. S. Heeschen & C. M. Wade (Dordrecht: Reidel), 163
Stone, J. M., Mihalas, D., & Norman, M. L. 1992, ApJS, 80, 819
Stone, J. M., & Norman, M. L. 1992a, ApJS, 80, 753
———. 1992b, ApJS, 80, 791
van Putten, M. H. P. M. 1996, ApJ, 467, L57
Wiita, P. J., Hooda, J. S., & Gopal-Krishna. 1997, Ap&SS, in press
Wiita, P. J., & Norman, M. L. 1992, ApJ, 385, 478
Wiita, P. J., Rosen, A., & Norman, M. L. 1990, ApJ, 350, 545 (WRN)
Zhao, J.-H., Burns, J. O., Hardee, P. E., & Norman, M. L. 1992a, ApJ, 387, 69
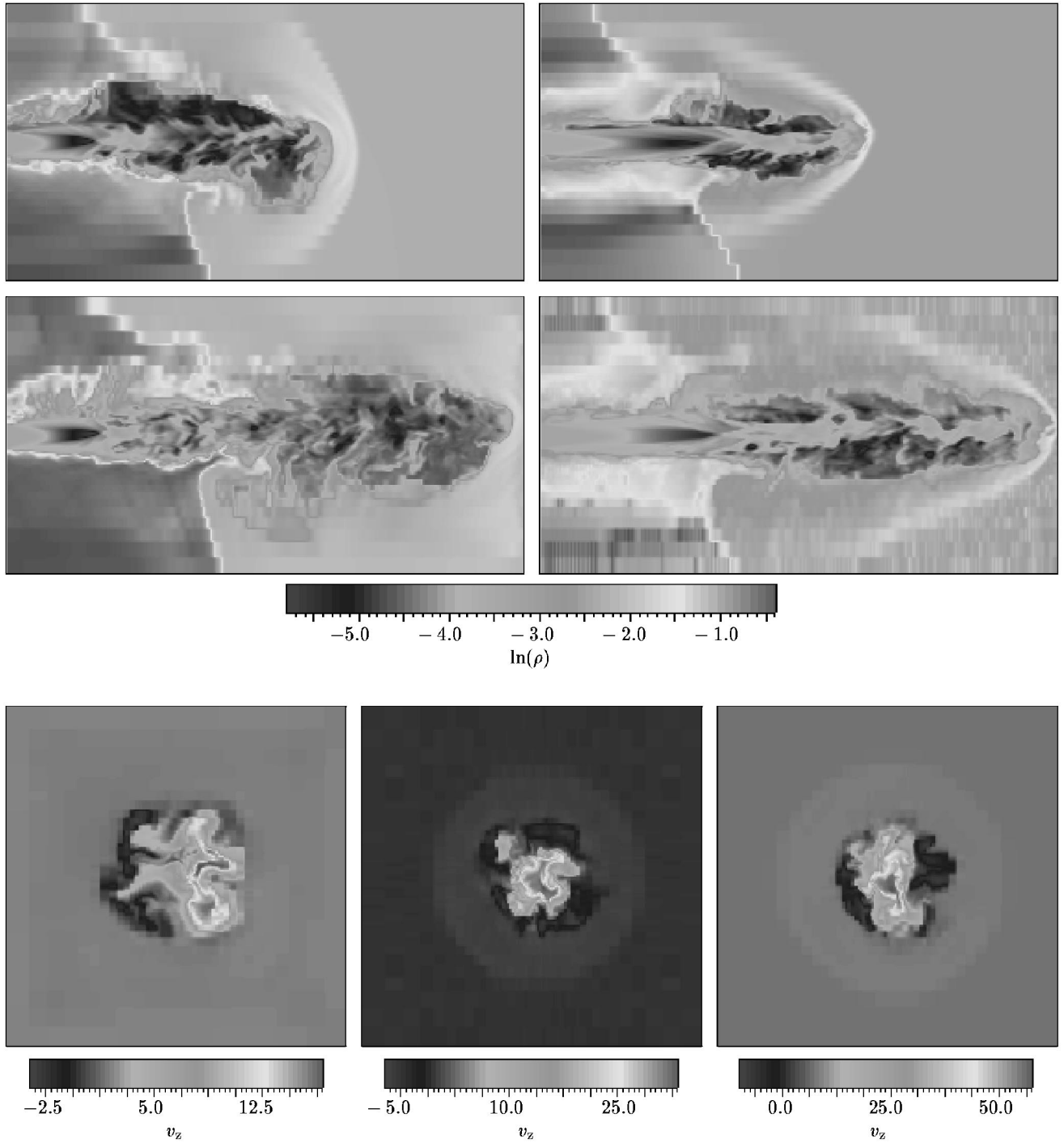Zhao, J.-H., Burns, J. O., Norman, M. L., & Sulkanen, M. E. 1992b, ApJ, 387, 83

FIG. 1.—Upper portion gives gray-scale logarithmic density plots for run M4 ($M_j = 3.0$; *left panels*) and M1 ($M_j = 6.0$; *right panels*). The other common parameters for these two runs are $\eta = 0.0316$, $z_H = 10.00R_0$, $\theta = 30°$, and $b = 0.75$. These images, which are slices in the x-z plane for $y = 0$ and cover the entire grid ($0 < z < 45R_0$; $-12R_0 < x < +12R_0$), are compared at $t = 8.4$ and 3.0 (*upper panel*), and at $t = 13.6$ and 4.6 (*middle panel*), respectively. The scale bar actually applies to an average of these longitudinal density slices. In the bottom figure, slices of v_z taken perpendicular to the jet at $z = 36.00R_0$ are compared for M4 (*left panel*), M1 (*middle panel*), and M7 (*right panel*) at $t = 13.2$, 4.6, and 4.6, respectively. (Simulation M7 differs from M1 only in the density ratio $\eta = 0.0100$.) These images cover $-12R_0 < x, y < +12R_0$.
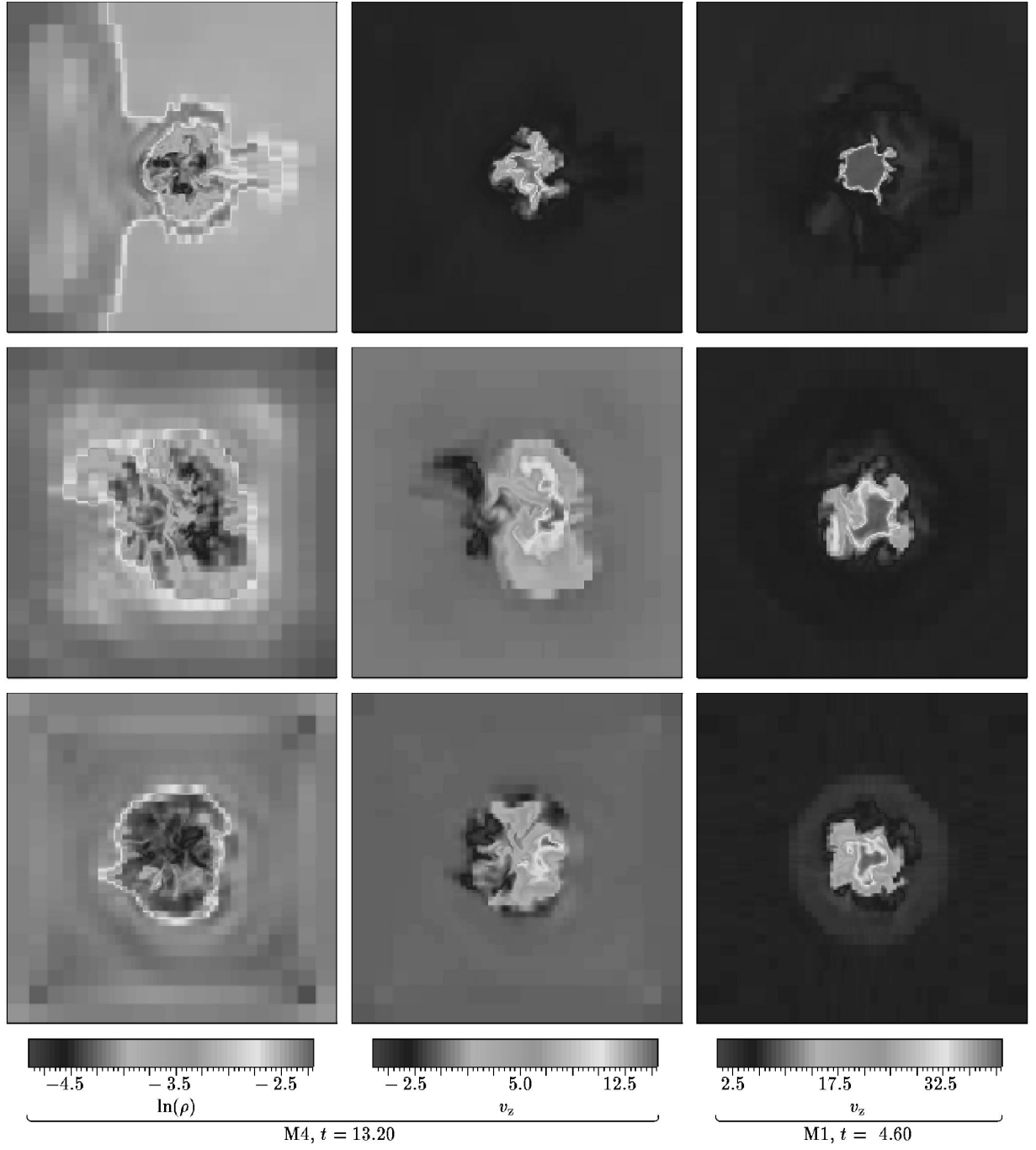
HOODA & WIITA (see 493, 83)

PLATE 5

Fig. 2.—Slices of ln (density) (*left panels*) and v_z (*central panels*) for run M4 ($M_j = 3.0$), and v_z (*right panels*) for run M1 ($M_j = 6.0$), taken perpendicular to the jet at $t = 13.20$ and $t = 4.60$, respectively (shortly after and just before, respectively, the bow-shock passed the end of the grid). The other common parameters are $\eta = 0.0316$, $\theta = 30°$, $b = 0.75$, and $z_H = 10.0$. The images are $12.00R_0 \times 12.00R_0$ wide and are sliced at distances of $z = 16.02R_0$ (*upper panels*), $30.42R_0$ (*middle panels*), and $39.42R_0$ (*bottom panels*). The scale bars apply exactly only to the bottom panels and approximately to the upper and middle panels.
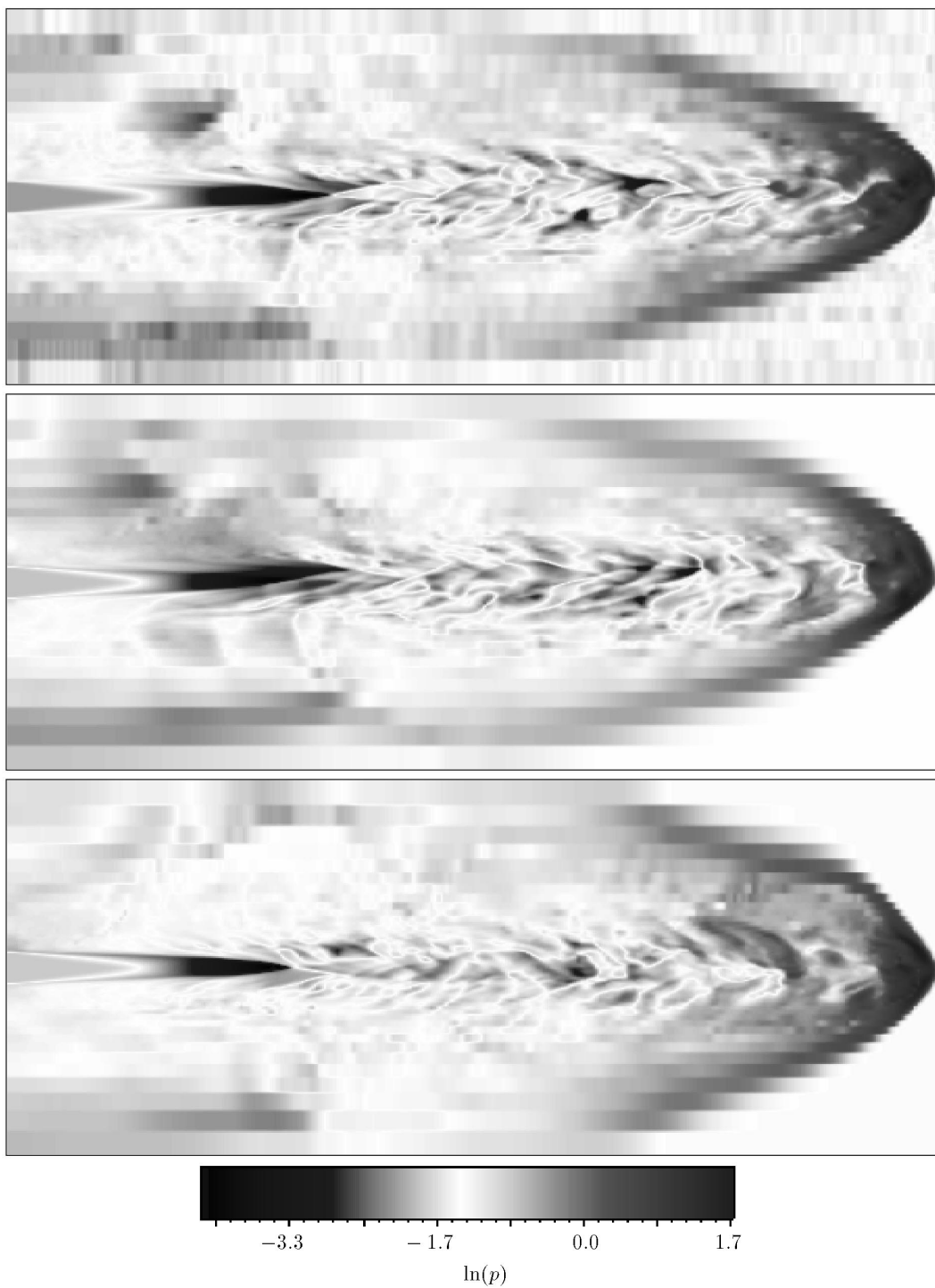
HOODA & WIITA (see 493, 83)

PLATE 6

Fig. 3.—Images of $\ln(p)$ for runs M1 (*upper panel*), M5 (*middle panel*), and M7 (*bottom panel*), with $\eta = 0.0316$, $\theta = 30°$; $\eta = 0.0316$, $\theta = 45°$; and $\eta = 0.0100$, $\theta = 30°$; respectively ($M_j = 6.0$, $b = 0.75$, and $z_H = 10.00R_0$ are common). The x-z slices are in the $y = 0$ plane at time $t = 4.6$. The scale bar applies in an average sense to these pressure images.

Hooda & Wiita (see 493, 84)

PLATE 7